Structures *in* Fire

Proceedings of the Ninth International Conference

Organized by Princeton University

Edited by

Maria E. Moreyra Garlock
Venkatesh K.R. Kodur

DES*tech* Publications, Inc.

Structures in Fire

DEStech Publications, Inc.
439 North Duke Street
Lancaster, Pennsylvania 17602 U.S.A.

Printed in the United States of America
10 9 8 7 6 5 4 3 2 1

Main entry under title:
Structures in Fire (Proceedings of the Ninth International Conference)

A DEStech Publications book
Bibliography: p.
Includes index p. 1141

ISBN: 978-1-60595-320-5

Preface

The "Structures in Fire" (SiF) specialized workshop series was conceived in the late 1990's with the first international workshop hosted in Denmark in 2000. SiF workshops followed every two years: New Zealand (2002), Canada (2004), and Portugal (2006). These events were renamed as International *Conferences* on Structures in Fire and held in Singapore (2008), the United States (2010), Switzerland (2012) and Shanghai (2014). Princeton University, USA, was selected to host the 2016 SiF International Conference (SiF'2016) from June 8 to June 10.

The main mission of SiF conferences is to provide an opportunity for researchers, practitioners and engineers to share their "Structures in Fire" research, technology, and expertise with their peers in an international forum. Allowing papers to be submitted only two months before the conference permits the most current scholarship to be presented. In addition to high quality state-of-the-art presentations, the 2016 SiF conference places significant value on discussions at the conference, both formally following presentations, and informally through social gatherings.

SiF'2016 received about 250 abstracts for consideration. The Scientific Committee made three reviews of each abstract, and based on their recommendations about 150 papers were invited for publication, from which 135 accepted the invitation. These proceedings represent those 135 papers, and collectively they represent the international state-of-the art in fundamental knowledge and practical applications of structural fire safety. Twenty-six countries from around the globe have contributed to the knowledge contained in this book.

In these proceedings, the papers are grouped into the following categories:

- Concrete Structures
- Concrete Structures: Fiber Reinforcement and Strengthening
- Concrete Structures: Material Behavior
- Metal Structures
- Metal Structures: Connections and Composite Floors
- Metal Structures: Material Behavior
- Composite Columns
- Timber Structures
- Material Behavior

- Bridges and Non-buildings Structures
- Experimental Methods
- Probabilistic Approaches and Applications of Fire Safety
- Numerical Modeling
- Fire Protection

We hope that the work presented in these proceedings will lead to safer, more economical, and more elegant fire designs for structures.

We extend a sincere 'thank you' to the Steering Committee for their guidance in making important decisions regarding the program format and proceedings. Our appreciation also goes to the members of the Scientific Committee for dedicating their time reviewing the abstracts. We are grateful to the Organizing Committee who was instrumental in developing the conference program and website. We also appreciate the work of Conference Services at Princeton University, in particular Lucy Weise, for managing registrations, classroom reservations, catering, etc. A huge thank you goes to the staff in the Civil and Environmental Engineering Department at Princeton University, in particular Jillian Hoffman and Islam Elnaggar, for supporting abstract and paper submissions, visa letters, attending to emails and a lot of other secretariat support.

Of course, SiF'2016 would not be possible without the proceeding's authors and conference participants. To you, we extend our greatest appreciation for making SiF'2016 a success.

Maria E. Moreyra Garlock
Chair, Organizing Committee
Princeton University

Venkatesh K. R. Kodur
Chair, Scientific Committee
Michigan State University

Scientific Committee

Chairman: Venkatesh Kodur, Michigan State University, USA

Tony Abu, University of Canterbury, New Zealand
Faris Ali, University of Ulster, Ireland
Pradeep Bhargava, Indian Institutes of Technology, Roorkee, India
Luke Bisby, University of Edinburgh, Scotland
Florian Block, Buro Happold, Germany
Andy Buchanan, University of Canterbury, New Zealand
Ian Burgess, University of Sheffield, England
Suwen Chen, Tongji University, China
Frank Dehn, Leipzig University, Germany
Dionis Dhima, Centre Scientifique et Technique du Batiment (CSTB), France
Michael D. Engelhardt, University of Texas at Austin, USA
Roberto Felietti, Politecnico di Milano, Italy
Mario Fontana (Track Leader), Swiss Federal Institute of Technology in Zurich, Switzerland
Massimo Fragiacomo, University of Sassari, Italy
Andrea Frangi, Swiss Federal Institute of Technology in Zurich, Switzerland
Jean-Marc Franssen, University de Liège, Belgium
Pietro Gambarova, Polytechnic University of Milan, Italy
Leroy Gardner, Imperial College, England
Maria Garlock, Princeton University, USA
Martin Gillie, University of Manchester, England
Mark Green, Queen's University, Canada
John Gross, National Institute of Standards and Technology (NIST), USA
Ralph Hamerlinck, Bouwen met Staal, Netherlands
Linhai Han, Tsinghua University, China
Zhaohui Huang, Brunel University, England
Basam Izzuddin, Imperial College, England
Marc Janssens, South West Research Institute, USA
Ann Jeffers, University of Michigan, USA
Daniel Joyeux, Efectis, France
Markus Knobloch, Swiss Federal Institute of Technology in Zurich, Switzerland
Susan Lamont, Arup, England
Angus Law, The University of Queensland, Australia
Guo Quiang Li (Track Leader), Tongji University, China
Mahen Mahendran, Queensland University of Technology, Australia
C. S. Manohar, Indian Institute of Science, India
Vasanth Matsagar, Indian Institutes of Technology, Delhi, India
Ali Nadjai, University of Ulster, Ireland
Emidio Nigro, University of Naples Federico II, Italy
Jyri Outinen, Ramboll, Finland
Spencer Quiel, Lehigh University, USA

João Paulo Rodrigues, Universidade de Coimbra, Portugal
Peter Schaumann, University of Hannover, Germany
Joachim Schmid, SP Technical Research Institute, Sweden
Mahmood Tabaddor, Underwriters Laboratory, USA
Luc Taerwe, University of Ghent, Belgium
Didier Talamona, University of Newcastle, Australia
Philip Tan Kang Hai (Track Leader), Nanyang Technological University, Singapore
Asif Usmani (Track Leader), Brunel University, England
Amit Varma, Purdue University, USA
Olivier Vassart, Arcelor Mittal, Luxembourg
Paulo Vila Real (Track Leader), University of Aveiro, Portugal
Frantisek Wald, Czech Technical University in Prague
Yong C. Wang, University of Manchester, England
Bo Wu, South China University of Technology (SCUT), China
Yao Yao, Northwestern Polytechnic University, USA
Raul Zaharia, University of Timisoara, Romania
Bin Zhao (Track Leader), Centre Technique Industriel de la Construction Métallique (CTICM), France
Huang Zhaohui, Brunel University, England

Organizing Committee

Maria E. Moreyra Garlock, Chair, Princeton University, USA
Jonathan Glassman, Exponent Failure Analysis Associates, USA
Negar Elhami Khorasani, University at Buffalo-SUNY, USA
Spencer Quiel, Lehigh University, USA

Steering Committee

Andy Buchanan, University of Canterbury, New Zealand
Jean-Marc Franssen, University of Liege, Belgium
Paulo Vila Real, University of Aveiro, Portugal
Venkatesh Kodur, Michigan State University, USA

Acknowledgements

Glass Fibre Reinforced Polymer (GFRP) Reinforced Concrete Slabs with Low Cover in Fire

HAMZEH HAJILOO[1], MARK F. GREEN[1],
NOUREDDINE BÉNICHOU[1] and MOHAMED SULTAN[2]

SUMMARY

One of the main safety requirements in the design of buildings is ensuring safe and appropriate fire endurance of the structures. To fill the knowledge gap on the fire resistance of fibre reinforced polymer (FRP) reinforced concrete members, comprehensive experimental and analytical studies are underway at Queen's University with collaboration from industry and the National Research Council of Canada (NRC). As a part of the program, two full-scale glass FRP (GFRP) reinforced concrete slabs were tested under exposure to the ASTM-E119 standard fire. The slabs were identical except that they were reinforced with different types of GFRP and tested to examine the adequacy of 40 mm of clear concrete cover. Currently, CSA-S806 allows a simplified method to design concrete slabs with FRP reinforcement and this results in a requirement for clear concrete cover of approximately 60 mm to achieve a 2 hour fire resistance rating. The test results showed that the slabs endured beyond 3 hours of fire exposure while resisting a high level of sustained load that was higher than the expected service load.

INTRODUCTION

It is generally supposed that concrete elements with FRP reinforcing bars have lower fire resistance than equivalent conventionally reinforced concrete with steel. In fact, until last year, the *ACI Guide for the Design and Construction of Concrete Reinforced with FRP Bars* [1] did not recommend FRP reinforcement for structures in which fire resistance was vital to maintain structural integrity. Design of FRP reinforced concrete members to resist fire incidents has been challenging since the available standards such as CSA-S806 [2] propose thicker concrete cover than the required cover for steel reinforced elements. Given the higher short-term construction cost of FRP reinforced structures than for steel reinforced ones, thicker concrete cover to ensure fire resistance, which leads to inefficient material use in FRP reinforced

[1]NRC-construction, National Research Council Canada, Ottawa, ON, Canada
[2]Civil Engineering, Queen's University, 58 University Avenue, Kingston ON Canada

construction, has limited applications of FRP reinforcement in structures where fire is a concern. This uncertainty excludes FRP reinforcement from many applications such as parking garages where FRP reinforcement can ensure durability of the structures. FRP reinforcement is a competitive replacement for steel in bridge construction; however, recent fire incidents have also created needs to consider fire in bridge design.

The authors, in collaboration with industry partners, have launched an extensive research program on the evaluation of FRP material behaviour at elevated temperatures and FRP reinforced concrete flexural elements to address these issues. As a part of this project, two full-scale slabs were tested in the floor furnace at the National Research Council (NRC) facilities. The slabs were designed and fabricated to represent common FRP reinforced concrete slabs such as those found in a typical parking garage but with only 40 mm of clear concrete cover.

EXPERIMENTAL PROGRAM

The intent of this experiment was to achieve two hours of fire endurance with 40 mm cover for simply supported unrestrained slabs under standard fire exposure. The slabs were heavily instrumented to collect the thermal field data in exposed and unexposed areas of slabs. Strain gauges were installed on the longitudinal reinforcing bars to measure strain before fire test and during the early stages of the fire test.

Two concrete slab specimens were fabricated for this experimental test; each was reinforced with reinforcing bars from a different manufacturer, which are designated as Slab-A and Slab-B hereafter. The slabs were conservatively tested without end restraints and were free to rotate and expand. Table I provides the details of the specimens.

The slabs were 3900 mm long, 1200 mm wide, and 200 mm thick which is typical for slabs in parking garages. The clear concrete cover to the bottom of longitudinal reinforcing bars was 40 mm. The centre-to-centre clear spacing of the bottom and top longitudinal reinforcement was 150 and 220 mm, respectively. The transverse reinforcing bars were placed in 200 mm intervals at the bottom and top meshes to control shrinkage and thermal cracks. Concrete with carbonate aggregate was used in the fabrication of slabs with the average 28 day compressive strength of f_c' = 34 MPa.

The GFRP reinforcing bars for the slabs had a nominal diameter of 16 mm. Rebar-A had sand coating on the surface which was applied on the hardened reinforcing bar following the pultrusion process. Rebar-B had a helical braid of fibres was in addition to a sand coating. This braid created surface deformations to enhance bond. Properties of the GFRP reinforcing bars are given in Table II.

Table I. FABRICATION DETAILS FOR THE SLABS.

Slab ID	Thickness (mm)	Cover (mm)	Reinforcement	Aggregate	f_c' (MPa)
Slab-A	200	40	Rebar-A	Carbonate	34
Slab-B	200	40	Rebar-B	Carbonate	34

Table II. MANUFACTURER SPECIFIED MATERIAL PROPERTIES.

Properties	Units	Rebar-A	Rebar-B
		#5	#5
Nominal Diameter	(mm)	16	16
Nominal Cross Sectional Area	(mm^2)	198	199
Nominal Tensile Strength	(MPa)	1720	1290
Nominal Modulus of Elasticity	(MPa)	64100	62600
Glass transition temperature	°C	119	114

Test Configuration and Procedure

The NRC's floor furnace can accommodate two centered slabs next to each other with the space between them filled by ceramic insulating blankets. The uniformly distributed load was applied by a loading system comprised of six jacks located on each slab. The superimposed load was constant during the fire test until failure occurred. The slabs were tested under a sustained distributed load of 19.1 (kN/m) which resulted in a bending moment equal to approximately 45 kN.m, which corresponded to 45 % of the ultimate flexural capacity of the slabs based on the tested 28 day strength of the concrete.

In most fire experiments, the ASTM E119 [3] or the ISO-834 [4]standard fire curves are used to evaluate the fire resistance of reinforced concrete members incorporating FRPs. Both curves are suitable for fire testing of structural elements. In this project, the ASTM E119 standard fire curve was used, and the temperatures inside of furnace were monitored using nine thermocouples located as close as possible to the bottom surface of the specimens. Following closely the ASTM E119 fire curve, the temperature increases rapidly during their early stages and stabilizes at around 1000 °C, reaching 1050 °C after three hours.

TEST RESULTS

Both concrete and reinforcing materials are influenced when subjected to fire. Although the degradation of concrete and steel reinforcement in conventional reinforced concrete elements is a matter of concern, concrete is not as much of a concern for FRP reinforced members since the degradation of the FRP material takes at lower temperatures than those that negatively affect concrete.

The thermal distribution in the slabs was recorded using 29 thermocouples placed in each slab. The temperatures throughout the concrete depth at midspan of Slab-B are shown in Figure 2.

Thermocouple T21 was located very close to the bottom surface of the slabs and hence the highest temperatures were recorded by T21. The recorded temperatures in the first five minutes of the fire were close to the internal furnace temperatures and reached 135 °C in 5 minutes. A notable spike in T21 at 75 minutes was due to local spalling of concrete leaving the thermocouple with less cover. The second thermocouple, T22, located 20 mm deep into the slab, reached 135 °C in 11 minutes. T23, located at the level of the reinforcing bars, showed that temperature on the bars was 365 °C after 2 hours of fire exposure. Material tests have shown that the FRP reinforcing bars retain approximately 40 % of their room temperature strength at a temperature of 365 °C [5].

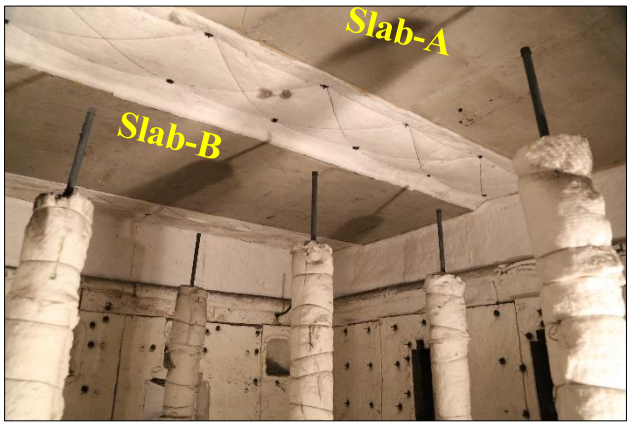

Figure 1. Testing furnace and setup

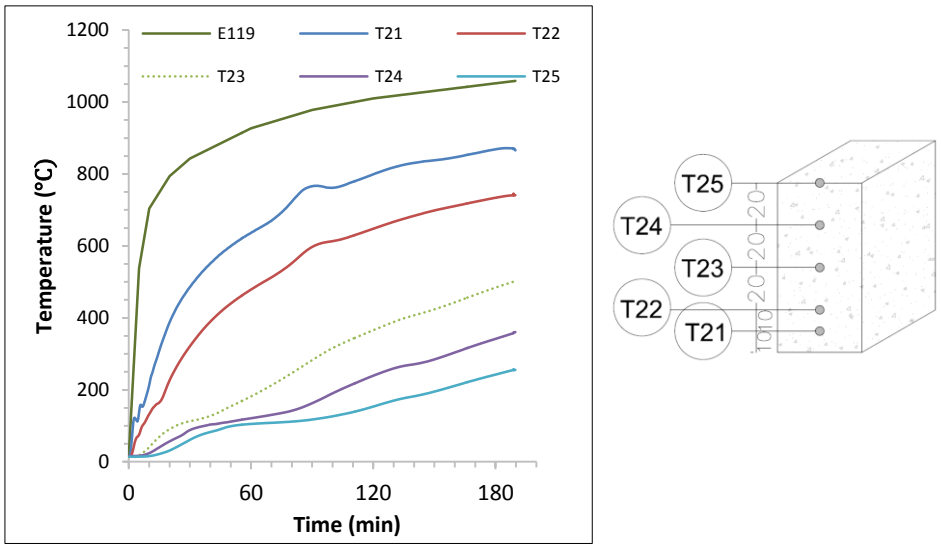

Figure 2. Temperatures within the thickness of Slab-B.

T23 and T24 were located at 40 and 60 mm from the exposed bottom surface of slab, respectively. Considering that the outer diameter of the reinforcing bars was approximately 20 mm, the readings of T23 and T24 were representative of temperatures at the bottom and top surfaces of the reinforcing bars. While the temperature increased in the bottom of the lower reinforcement layer to 365 °C after two hours of exposure, thermocouple T24 (close to the top surface of the reinforcing bars in the bottom of the slab) showed only 240 °C demonstrating a thermal gradient of approximately 125 °C across the reinforcing bars. Such differences between temperatures on the top and bottom surfaces of the reinforcing bars were observed during the entire fire exposure.

In steel reinforced structures, the bond strength variation at elevated temperature is quite similar to the variation in the compressive strength of the concrete [6]. However,

the bond of FRP reinforcement to concrete deteriorates at lower temperatures and when the temperature at the FRP to concrete interface reaches about 170 °C, the remaining bond strength is approximately 10% of the bond strength at room temperature for both Rebar-A and Rebar-B [7]. Thus, the most informative thermal data were collected from the anchor zone where eight thermocouples were aligned along 200 mm of the anchor zone (Figure 3). These thermocouples recorded the thermal gradients along the reinforcing bars in the anchor zone. These areas of interest were heavily instrumented since the failure of the slabs was expected to initiate by bond degradation between the FRP and concrete based on a previous set of fire tests on GFRP reinforced slabs [8]. All of the thermocouples illustrated in Figure 3 were installed at a depth of 40 mm into the thickness of the slab at the bottom surface of the reinforcing bars. The first thermocouple was placed 25 mm from the end of slabs and the rest of thermocouples were located every 25 mm; the last sensor (T11) was located on the boundary of the exposed and protected area.

The thermal field in the anchor zone at the ends of Slab-A and Slab-B is shown in Figure 4. The recorded results in Figure 4 show that the temperatures remained below 100 °C at 75 mm (T16) from the ends of Slab-A during the test; the maximum temperature at the same location for Slab-B was 116 °C. At these temperatures, the bond strength between the concrete and the FRP was approximately 30 % of the room temperature strength.

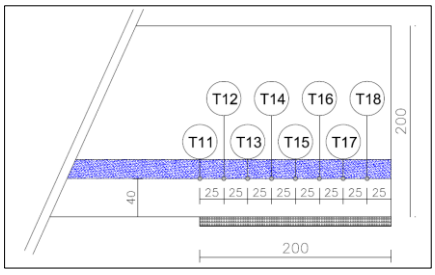

Figure 3. Thermocouples placed in the anchor zone of each slab.

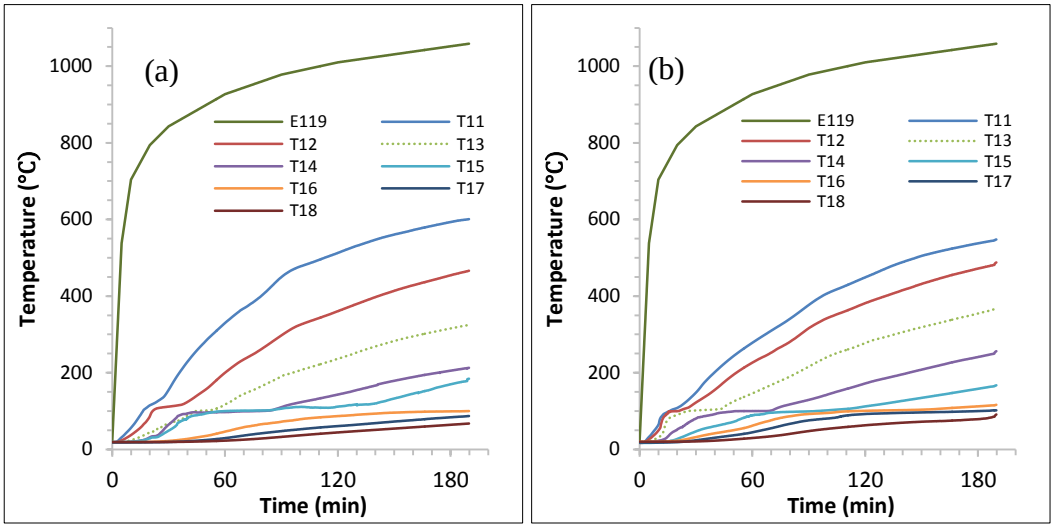

Figure 4. Temperature variations in the anchor zone; (a) Slab-A; (b) Slab-B.

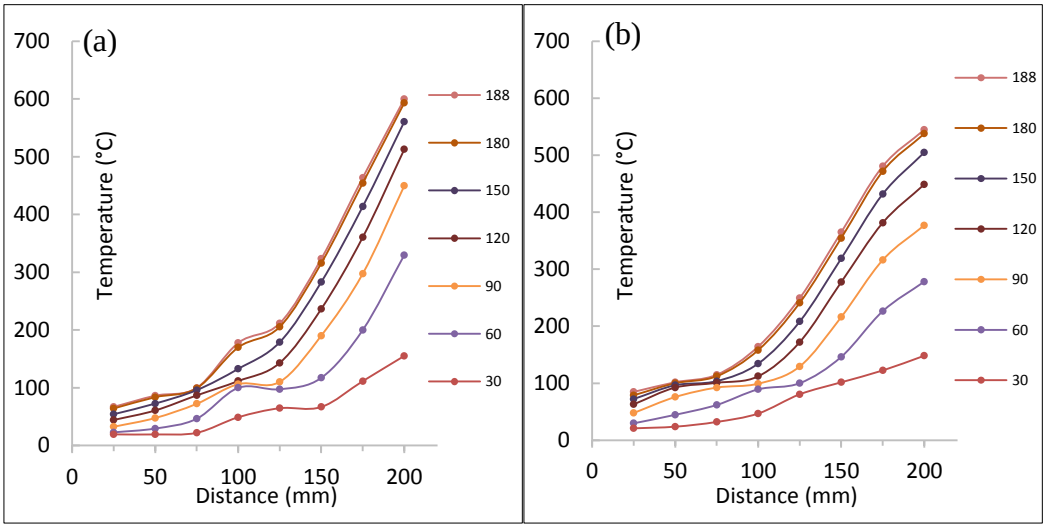

Figure 5. Temperature gradients along the anchor zone; (a) Slab-A; (b) Slab-B.

Figure **5** shows thermal gradients in the anchor zone. Temperatures drop significantly from the edge of the exposed zone towards the unexposed zone, especially between the 200 mm and 125 mm away from the end of the slabs. The thermal field becomes uniform in the last 100 mm strip of the slabs.

Failure modes

According to ASTM E119-15 [3], the average temperature rise of the unexposed surface of the slab with respect to the room temperature has to remain below 139 °C. In addition, passage of flame through the slab is not permitted. None of these failure criteria associated with thermal behaviour occurred during the fire exposure.

Both slabs were able to carry a high level of superimposed load for more than 180 minutes. It should be noted that the load applied on the slabs during fire exposure was well beyond the expected load on the slabs in a real fire incident. Since serviceability governed the design of the slabs, the corresponding expected service moment was 23.4 kN.m. Despite this, the slabs endured more than three hours of fire exposure under a higher sustained moment of 45 kN.m that corresponded to 45 % of the ultimate flexural capacity of the slabs based on the tested 28 day strength of the concrete.

The slabs were simply supported at the ends and unrestrained axially and rotationally before load application and during fire exposure. Figure 6 shows the time–deflection behaviour of the slabs after the start of the fire. Uneven thermal fields in the lower and top layers of concrete caused the slabs to bow downward. The deflection shown in Figure 6 consisted of the heat-induced bowing deflections and deflections due to the fact that the concrete and FRP reinforcing bars were degrading as a result of elevated temperatures during fire exposure. The changes in temperatures at the lower layers of concrete too place quickly. As shown in Figure **6**, thus, there was a rapid deformation in first 20 minutes of the onset of fire. Then, the time-deflection curve reached an almost stable region. After 60 minutes, the temperatures at the bottom of the reinforcing bars reached 180 °C, and as mentioned earlier from the material tests [7], the remaining bond strength of the reinforcing bars in the centre of the slabs was small. However, the relatively short embedment of the reinforcing bars into the anchor zone still provided sufficient bond strength between the reinforcing bars and concrete. In other words, the slabs were anchored from both ends acting like a tied arch. This change in structural behaviour from a bonded to an unbonded system caused rapid increase in the deflection.

After two hours, the slabs deformed at a relatively higher rate, especially Slab-B. Right after three hours (at 188 minutes), Slab-B failed due to excessive deflection, and the test was stopped to prevent it from falling into the furnace. Figure 7 shows the excessive residual deflection of Slab-B after the fire test.

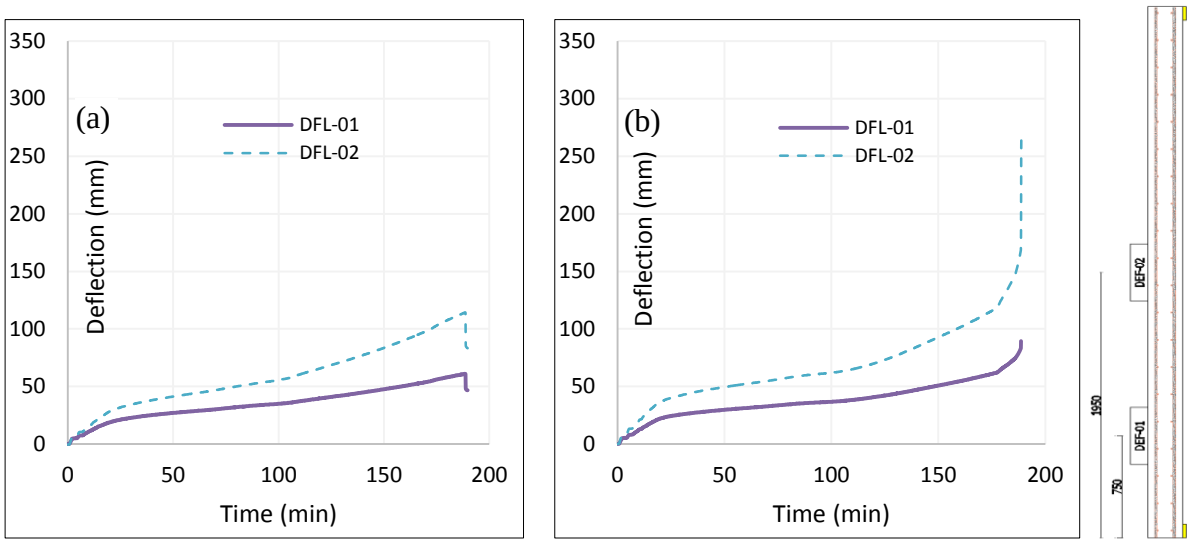

Figure 6. Deflection vs time; (a) Slab-A and (b) Slab-B.

Figure 7. Excessive deflection of Slab-B.

CONCLUSIONS

By virtue of the results of these fire tests, another step was taken towards constructing FRP reinforced concrete structures with more certainty by demonstrating safe applications of FRP reinforcing bars with relatively low concrete cover. The tests investigated the fire safety of the very efficient practice of GFRP reinforcement in flexural elements with only 40 mm of clear concrete cover. The results proved that FRP flexural elements can endure more than three hours and that 200 mm embedment of the bars into the support is sufficient to prevent early failure due to bond loss.

ACKNOWLEDGEMENTS

The authors would like to thank the Natural Sciences and Engineering Research Council of Canada (NSERC), Pultrall Inc. and BP Composite for their financial and material support. The authors also appreciate the contributions of Patrice Leroux and the other technical staff of the Fire Research Laboratory at NRC, the insightful advice of Dr. B. Benmokrane, and the cooperation of Dr. H. Mohammad and the technical

staff at the University of Sherbrooke. The assistance of Dr. J. Gales (Carleton University) and Dr. M. Noël (University of Ottawa) is also appreciated.

REFERENCES

1. ACI-440.1R-15, Guide for the Design and Construction of Concrete Reinforced with FRP Bars in *American Concrete Institute, Detroit, Michigan*. 2015.
2. Canadian Standards Association, Design and construction of building components with fiber-reinforced polymers, in *Canadian Standards Association. Mississauga, Ontario, Canada:* 2012.
3. ASTM E119-15, Standard Test Methods for Fire Tests of Building Construction and Materials. 2015: ASTM International, West Conshohocken, PA.
4. ISO 834-11. Fire resistance tests- Elements of building construction. International Organization for Standardization.
5. Hajiloo, H., J. Gales, M. Noël, and M.F. Green. "Material Characteristics of Glass Fibre Reinforced Polymer (GFRP) Bars at High Temperature," presented at Protect 2015. 2015. Michigan, USA. pp. 94-104.
6. Harmathy, T.Z., *Fire safety design and concrete*. 1993: John Wiley & Sons, New York.
7. Hajiloo, H. and M.F. Green. "Bond Strength of Glass Fibre Reinforced Polymer Bars in Concrete at High Temperature," presented at CSCE-2015. 2015. REGINA, SK.
8. Hajiloo, H., M.F. Green, N. Bénichou, and M. Sultan. "Fire Performance of FRP reinforced concrete slabs " presented at 7th International Conference on Advanced Composite Materials in Bridges and Structures. 2016. Vancouver, Canada.

Creep Behavior of Flush Endplate Connections at Elevated Temperatures Due to Fire

AHMAD H. EL GHOR[1], ELIE G. HANTOUCHE[2], MOHAMMED ALI MOROVAT[3] and MICHAEL D. ENGELHARDT[4]

ABSTRACT

This paper highlights some preliminary results of a computational study investigating the effect of thermal creep of structural steel on the behavior of steel beam-column connections subjected to elevated temperatures due to fire. Through a series of finite element simulations that were partly verified against experimental data, a practical methodology was developed to investigate the time-dependent nature of the behavior of flush endplate beam-column connections at elevated temperatures. In this methodology, time effects on the strength and rotational capacity of flush endplate connections are explicitly presented in the form of isochronous force-rotation curves. The isochronous representation provides a possible framework for including creep effects in predicting the response of structural steel connections to fire.

INTRODUCTION

Flush endplate connections are one of the extensively used moment-resistant connections in steel buildings and steel portal frames due to economy and ease of construction. During a fire event, different components of the flush endplate connections can undergo significant loss of strength and stiffness. Large axial forces are also developed in these connections and the connecting beams as a result of restraints to thermal displacements [1]. These axial forces are initially compressive when beams expand during the initial heating stage of a fire. With increasing temperatures, these axial forces can become tensile as beams begin to sag and catenary action develops. Additional axial tensile forces are further developed as deflected beams contract during the cooling stage of a fire [2, 3].

[1]Graduate Student, Department of Civil and Environmental Engineering, American University of Beirut, Riad El-Solh 1107 2020, Beirut, Lebanon, Email: ahe26@mail.aub.edu
[2]Assistant Professor, Department of Civil and Environmental Engineering, American University of Beirut, PO Box 11-0236, Riad El-Solh 1107 2020, Beirut, Lebanon, Email: eh12@aub.edu.lb
[3]Research Scientist Associate, Department of Civil, Architectural and Environmental Engineering, Ferguson Structural Engineering Laboratory, The University of Texas at Austin, Austin, Texas 78758, Email: morovatma@utexas.edu
[4]Professor, Department of Civil, Architectural and Environmental Engineering, Cockrell School of Engineering, The University of Texas at Austin, Austin, Texas 78758, Email: mde@mail.utexas.edu

Moreover, steel flush endplate connections in fire are subjected to significant rotation demands. These large deformation and force demands combined with loss of strength can potentially result in the failure of flush endplate connections during and after a fire [1, 2, 3, 4].

There have been a number of attempts in the past to investigate the combined effects of shear and axial forces on the strength and rotational capacity of flush endplate connections subjected to fire [1, 2, 3, 4]. In these studies, both isolated connections under steady-state temperature conditions and connection sub-assemblies under transient-state temperature conditions were examined. A major observation from these studies was that the strength, rotational capacity, and failure modes of the flush endplate connections were significantly affected by temperature-dependent behavior of their components, mainly the endplate and the bolts [1, 2, 3, 4]. It is clear from these past observations that good understanding of mechanical properties of steel plates and bolts at elevated temperatures is crucial in accurately predicting the response of the flush endplate connections to fire.

The stress-strain behavior of structural steel at elevated temperatures has been shown to be highly time dependent for some ranges of stresses and temperatures expected during a building fire [5, 6]. Nonetheless, research on the effect of creep on the behavior of steel connections is quite meager [7].

In an effort to address this shortcoming, this paper proposes a methodology to characterize the time-dependent strength and deformation capacity of flush endplate connections when subjected to fire. It will be further shown how this methodology can be used in a performance-based framework to evaluate the performance of steel connections in fire.

THERMAL CREEP OF STRUCTURAL STEEL

Creep Phenomenon

Creep is defined as the time-dependent plastic strain under constant stress and temperature conditions. It is often stated that steel creep occurs when temperature of steel exceeds one-third to half of the steel melting temperature. The creep of steel is a complex phenomenon that depends on steel material type, applied stress, temperature, time duration, and stress and temperature histories. Creep curves, defined as strain versus time curves, are typically divided into the three phases of primary, secondary, and tertiary. In the primary stage, the curve is non-linear and exhibits a decreasing creep strain rate. In the secondary stage, the creep strain is almost constant. In the tertiary stage, the creep strain rate increases with time. For steel, the shape of the creep curve, the magnitude of the creep strain and the time scale are highly dependent on both the temperature and the stress levels [5, 6].

Creep of ASTM A36 Steel at Elevated Temperatures

Experimental and empirical models have been developed to predict creep strain of ASTM A36 steel at elevated temperatures [8, 9]. One of the widely used creep models in structural-fire engineering applications proposed by Fields and Fields [9]

incorporates a power law creep and represents creep strain, ε_c, in the form of a Norton-Bailey equation as follows:

$$\varepsilon_c = a\, t^b\, \sigma^c \qquad (1)$$

In this equation, t is time and σ is stress. The parameters a, b and c are temperature-dependent material properties. Fields and Fields [9] derived equations for these temperature-dependent material properties for ASTM A36 steel. The model developed by Fields and Fields [9] is capable of predicting creep in the temperature range of 350 °C to 600 °C and for creep strains up to 6-percent. The creep model by Fields and Fields [9] was used in the studies presented in this paper on the time-dependent response of steel flush endplate connections to fire.

TIME-DEPENDENT BEHAVIOR OF FLUSH ENDPLATE CONNECTIONS IN FIRE – DEVELOPMENT OF METHODOLOGY

In this section, a practical methodology developed to assess the time-dependent nature of the behavior of flush endplate beam-column connections in fire will be presented and explained. In this methodology, time effects on the strength and rotational capacity of flush endplate connections are explicitly presented in the form of isochronous force-rotation curves.

Flush Endplate Connection Prototype

The connection prototype selected for analysis followed the flush endplate connection details incorporated in the experiments conducted at University of Sheffield [10]. More specifically, as shown in Figure 1, the Flush endplate connection specimen used in the analysis consisted of a PL13×8×0.4 in. (PL332.4×200×10 mm) endplate, a W12×26 (UB305×165×40) beam, and a W10×60 (UC 254×254×89) column. Further, six grade 8.8 M20 bolts were used to connect the endplate to the column. Details of the connection configuration can be found in different publications from researchers at the University of Sheffield [1, 3, 10].

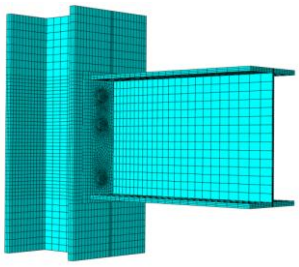

Figure 1. Flush endplate connection configuration used in simulations in Abaqus.

Important Modeling Considerations

An idealized bilinear stress-strain relation with isotropic hardening was used to model the mechanical behavior of both structural bolts and structural steel. The

ambient temperature properties incorporated in connection simulations were based on the reported values in the experimental work at University of Sheffield [1, 3, 10]. Retention factors proposed by researchers from the University of Texas at Austin [11] and University of Sheffield [12] were used to respectively model stress-strain characteristics of structural steel and structural bolts at elevated temperatures. To account for the time-dependent behavior of structural steel at elevated temperatures, a power law creep model proposed by Fields and Fields [9] was included in mechanical properties of structural steel used to model both the beam and the endplate. Thermal creep of structural bolts was ignored in connection simulations.

Development of Methodology

To develop the methodology, two series of finite element analyses were performed. In the first series, steady-state temperature analyses were conducted to characterize the strength of flush endplate connections under combined shear and tension forces at elevated temperatures. At each specific temperature (450 °C, 550 °C, and 650 °C), an inclined concentrated force (with the initial angle of 35°) was monotonically applied to the beam end with an angle varying throughout the loading step in accordance with the experimental protocol at University of Sheffield [10]. Figure 2 shows sample results of such analyses where experimental and finite element predictions of the strength of flush endplate connections are compared at various temperatures. As seen in Figure 2 and as shown in previous studies [1, 2, 3], finite element simulations are capable of predicting the experimental observations with reasonable accuracy. Note that due to the rapid loading protocol adopted in connection experiments at University of Sheffield [10], the strengths obtained in the first series of simulations were assumed to be time-independent and therefore thermal creep of steel was ignored in these simulations.

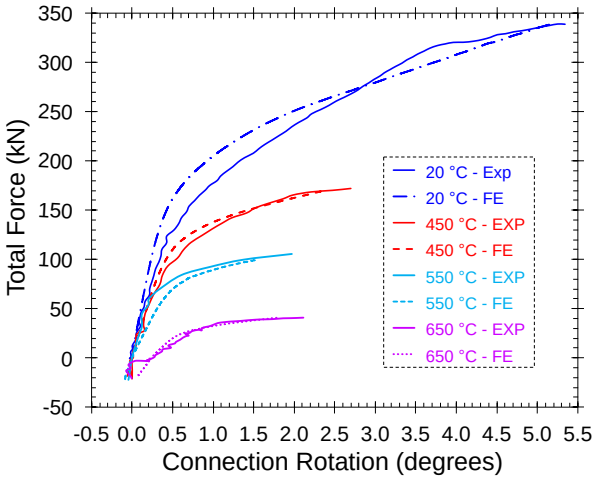

Figure 2. Time-independent strength of flush endplate connections at ambient and elevated temperatures.

In the second series, steady-state temperature creep tests were performed to investigate the creep response of flush endplate connections under combined shear and tension forces at elevated temperatures. More specifically, at each specific

temperature (450 °C, 550 °C, and 650 °C), an inclined force, equal to a fraction of the ultimate load predicted in the first series of analyses, was applied and kept constant throughout the test. Simulations were conducted for 240 minutes or until the connection failed. Representative results of creep tests at 550 °C and under various applied loads are depicted in Figure 3. As seen in Figure 3, connection rotations increased with time as a result of explicit consideration of thermal creep of structural steel in simulations. Further, the rate of increase in connection rotations was higher for larger applied loads.

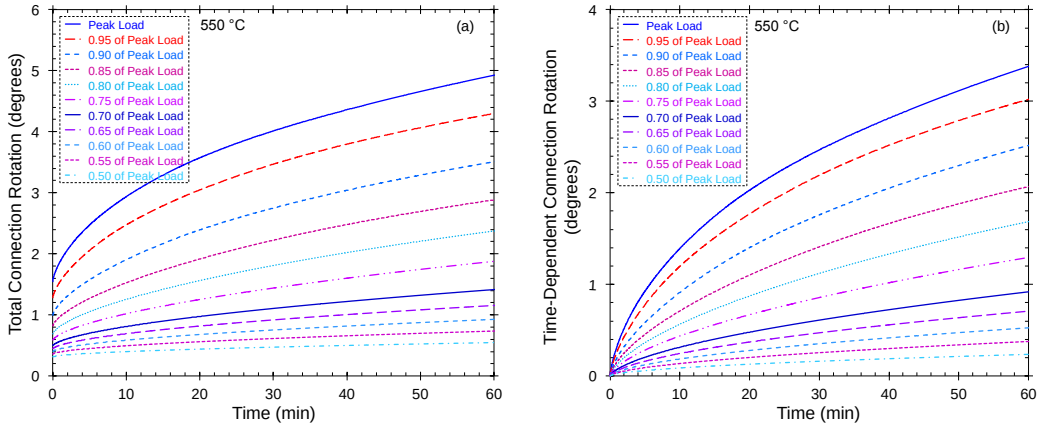

Figure 3. Effect of creep on the connection rotation at 550 °C.

Results obtained from steady-state temperature creep tests in the form of rotation versus time, like those shown in Figure 3, can alternatively be presented in the form of isochronous force-rotation curves. Figure 4 shows a sample of isochronous force-rotation curves corresponding to the creep test results shown in Figure 3. As can be seen in Figure 4, for any specific temperature like 550 °C, isochronous force-rotation curves are force-rotation curves at different time. In other words, they represent the time-dependent force-rotation response of the connection at any specific temperature. As further observed in Figure 4, compared to a single curve from connection experiments, isochronous force-rotation curves provide much richer insight into the connection behavior at elevated temperatures. It can be seen that at a specific time, larger connection rotation can be obtained for larger applied load.

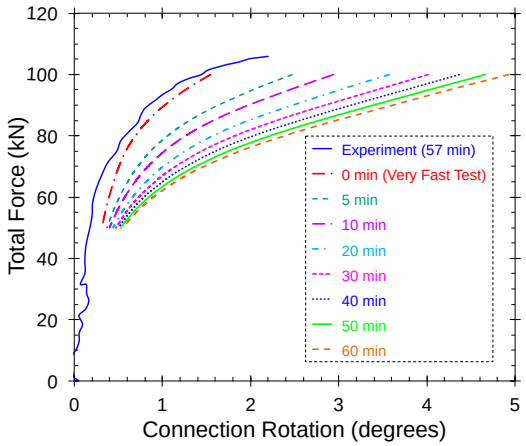

Figure 4. Isochronous force-rotation curves for the flush endplate connection in consideration at 550 °C.

TIME-DEPENDENT BEHAVIOR OF FLUSH ENDPLATE CONNECTIONS IN FIRE – APPLICATION OF METHODOLOGY

The methodology presented in the previous section to assess the time-dependent behavior of flush endplate connections subjected to fire temperatures can be used to study the behavior of flush endplate connections under more general conditions characteristics of the building fires such as variable temperatures.

Steady-state temperature creep tests, as explained previously, can be performed on the isolated flush endplate connection model in Abaqus under a constant applied load at different temperatures. If the results from these connection creep tests are combined in such a way that rotation-temperature points relating to the same time are connected to each other, the isochronous rotation-temperature curves will be constructed. A representative of these isochronous rotation-temperature curves for a constant load of 76 kN is depicted in Figure 5. Isochronous rotation-temperature curves such as the ones shown in Figure 5 simply indicate the time-dependent behavior of the flush endplate connections under transient-state temperature conditions characteristics of structural fires.

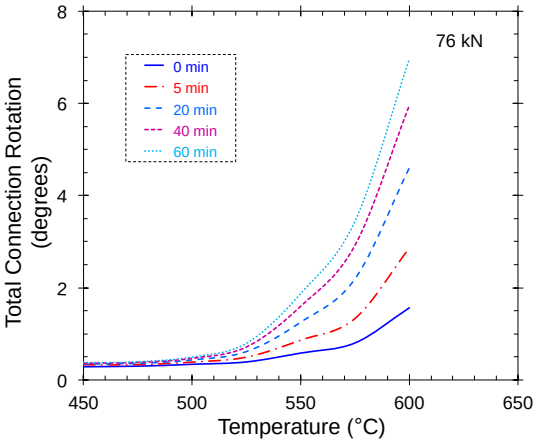

Figure 5. Isochronous rotation-temperature curves corresponding to the constant load of 76 kN.

The graphs shown in Figure 5 can further be represented in more general forms where the time-dependent behavior of flush endplate connections is presented under the conditions of variable loads and temperatures. Samples of such general isochronous rotation-temperature curves are shown in Figure 6. Note that eventhough curves in Figures 6(a) and 6(b) correspond to the ultimate loads and half of ultimate loads at each temperature, respectively, the actual loads are diferent from one temperature to the other (ultimate loads are the peak loads predicted in the first series of analyses where the creep effects are ignored).

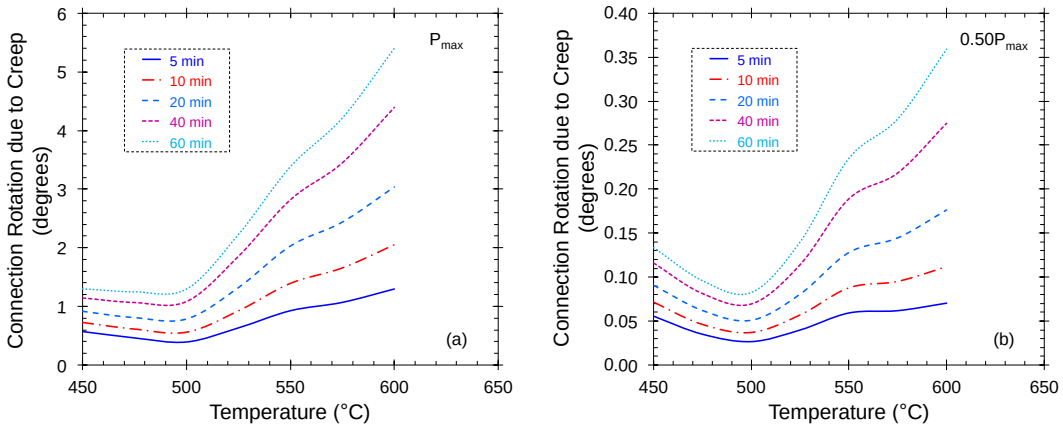

Figure 6. Isochronous rotation-temperature curves under variable loads.

An important observation from Figures 5 and 6 is that, according to the adopted creep model by Fields and Fields [9], the behvior of the selected flush endplate connection becomes highly time dependent for temperatures above about 500 °C. Figure 6 further shows that creep effect on the connection response to fire becomes more significant at higher applied loads.

Any time and temperature point on the isochronous rotation-temperature curves in Figures 5 and 6 can be related to a corresponding point on the design fire curve. This correspondence allows a designer to define the desirable performance levels for steel connections in terms of specific times or temperatures. In other words, the isochronous representations shown in Figures 5 and 6 can be utilized to define critical times and temperatures for designing connections in fire. This utilization can further provide a smooth transition from the current prescriptive-based approaches to the performance-based ones.

CONCLUDING REMARKS

Through a series of finite element simulations that were partly verified against experimental data, a practical methodology was developed to investigate the time-dependent nature of the behavior of flush endplate beam-column connections at elevated temperatures due to fire. In this methodology, time effects on the strength and rotational capacity of flush endplate connections are explicitly presented in the form of isochronous force-rotation curves. An example was provided of how the isochronous representation can be used to aid in the design of steel connections in

fire. The accuracy of the suggested methodology can be enhanced by considering more reliable creep models for structural steel at elevated temperatures, by including the thermal creep models for structural bolts, and by considering the constraints to thermal expansion and resulting stress relaxations.

ACKNOWLEDGMENTS

The authors gratefully acknowledge the financial support provided by the American University of Beirut Research Board under grant No.21113-102726, and by the Lebanese National Council for Scientific Research (LNCSR) under grant No. 103091-22968. The authors further would like to thank researchers at the University of Sheffield for making the connection test results publicly available.

REFERENCES

1. Yu, H., I. Burgess, J. Davison and R. Plank. 2011. "Experimental and Numerical Investigations of the Behavior of Flush End Plate Connections at Elevated Temperatures," *J. Struct. Eng.*, pp. 80-87.
2. Li, J.-T., G.-Q. Li, G.B. Lou and L.-Z. Chen. 2012. "Experimental Investigation on Flush End-plate Bolted Composite Connection in Fire," *J. Constr. Steel Res.*, pp. 121-132.
3. Al-Jabri, K .S., A. Seibib, and A. Karrech. 2008. "Modelling of Unstiffened Flush End-Plate Bolted Connections in fire," *J. Constr. Steel Res*., 62, pp. 151-159.
4. Li, G.-Q. and S.-X. Guo. 2008. "Experiment on Restrained Steel Beams Subjected to Heating and Cooling," *J. Constr. Steel Res.*, 64, pp. 268-274.
5. Morovat M.A., Lee J., Engelhardt M.D., Taleff E.M., Helwig T.A. and Segrest V.A. 2012. "Creep Properties of ASTM A992 Steel at Elevated Temperatures", *Advanced Materials Research*, 446-449, 786-792.
6. Morovat, M. A., J. Lee, M. D. Engelhardt, T. A. Helwig and E. M. Taleff. 2011. "Analysis of Creep Buckling of Steel Columns Subjected to Fire," *Structures Congress, ASCE*, pp. 2929-2940.
7. Kdour, V. K. R. and M. M. S. Dwaikat. 2010. "Effect of High Temperature Creep on the Fire Response of Restrained Steel Beams" *Materials and Structures*, 43, pp. 1327-1341.
8. Harmathy, T. Z.1967. "A Comprehensive Creep Model" *J. of Basic Eng., Trans. ASME*, 89(3), pp. 496-502.
9. Fields, B. A. and R. J. Fields. 1989. "Elevated Temperature Deformation of Structural Steel," *Report NISTIR 88-3899*, NIST, Gaithersburg, MD.
10. http://fire-research.group.shef.ac.uk/downloads.html, November, 2007.
11. Lee J., M .A. Morovat, G. Hu, M. Engelhardt, and E. Taleff. "Experimental investigation of mechanical properties of ASTM A992 steel at elevated temperatures," *Eng. J.*, 50(4), pp. 249-272.
12. Hu, Y., J. B. Davison, I. W. Burgess, and R.J. Plank. 2007. "Comparative Study of the behaviour of BS 4190 and BS EN ISO 4014 bolts in fire," *Proc., ICSCS* , Taylor & Francis, London, pp. 587-592.

Temperature and Strain Measurements with Fiber Optic Sensors for Steel Beams Subjected to Fire

YI BAO[1], YIZHENG CHEN[1], MATTHEW S. HOEHLER[2], CHRISTOPHER M. SMITH[2], MATTHEW BUNDY[2] and GENDA CHEN[1,*]

ABSTRACT

This paper presents measurements of high temperatures using a Brillouin scattering based fiber optic sensor and large strains using an extrinsic Fabry-Perot interferometric sensor for assessing the thermo-mechanical behaviors of simply-supported steel beams subjected to combined thermal and mechanical loading. The distributed fiber optic sensor captures detailed, non-uniform temperature distributions that are compared with thermocouple measurements resulting in an average relative difference of less than 5 % at 95 % confidence level. The extrinsic Fabry-Perot interferometric sensor captures large strains at temperatures above 1000 °C. The strain results measured from the distributed fiber optic sensors and extrinsic Fabry-Perot interferometric sensors were compared, and the average relative difference was less than 10 % at 95 % confidence level.

INTRODUCTION

During a fire, the load capacity and stability of steel structures can significantly degrade due to adverse temperature-induced deformations and reduced material properties [1]. To assess the thermo-mechanical conditions of a structure, both temperatures and strains must be known. The current state of practice in experimental fire testing is to measure the temperature and global deformation of specimens and to use analytical models to understand the behavior of the member. Effective tools are lacking to directly measure strains in steel members subjected to fire, reliably and accurately.

Fiber optic sensors have drawn intense research interest in the past decade due to their unique advantages, such as immunity to electromagnetic interference, small size, light weight, and excellent durability and resistance to harsh environments. However, their application to structures in fire has not yet been fully explored. Conventional grating-based fiber optic sensors degrade significantly when heated over 300 °C and typically fail around 600 °C [2], which limits their application in fire. Although their temperature operation range can be increased to 1000 °C through means such as the regenerated fiber Bragg grating technique [2], the grating sensors do not provide spatially distributed measurements, but rather a point

Department of Civil, Architectural, and Environmental Engineering, Missouri University of Science and Technology, 1870 Miner Circle, Rolla, MO 65409, USA
National Fire Research Laboratory, National Institute of Standards and Technology, 100 Bureau Drive, Stop 8666, Gaithersburg, MD 20899, USA
*Corresponding to Dr. Genda Chen. Email: gchen@mst.edu, Phone: (573)341-4462

measurement at the grating location. In contrast, fully-distributed fiber optic sensors provide a more detailed picture of the structural thermal field. Based on Brillouin scatterings in optical fiber, Brillouin Optical Time Domain Analysis and Brillouin Optical Time Domain Reflectometry technologies have been developed to measure strain and temperature distributions [3]. However, their spatial resolutions were typically limited to half a meter or larger, which is not precise enough in many applications. Recently, a pulse pre-pump Brillouin Optical Time Domain Analysis (PPP-BODTA) technology was developed with a 2 cm spatial resolution [4].

In this study, distributed fiber optic sensors with PPP-BODTA [5] and extrinsic Fabry-Perot interferometric (EFPI) sensors [6] are employed to measure temperatures and strains in steel beams exposed to fire. The sensors' accuracies and precisions for temperature and strain measurements are compared and evaluated.

WORKING PRINCIPLES

The working principles of the distributed fiber optic sensor and extrinsic Fabry-Perot interferometric sensor are briefly introduced in this section. In this study, all fiber optic sensors were fabricated using telecommunication-grade fused silica single-mode fibers. The fiber cross section consisted of an 8.2 μm glass core and a 125 μm glass cladding [7]. Typically, optical fibers are coated with protective polymer coatings outside of cladding to enhance the mechanical performance [8]. In this study, for strain measurement, the coatings were removed before the fibers were installed on the test specimens. However, for temperature measurement, the coatings could be left and burned off at about 300 °C to 400 °C [9].b

Distributed Fiber Optic Sensor

In this study, PPP-BOTDA based on stimulated Brillouin scatterings in optical fiber was employed. Stimulated Brillouin scatterings result from the interactions between light waves and acoustic waves in optical fiber [2]. PPP-BOTDA measures the Brillouin frequency shift along the optical fiber, which is related to the strain and temperature changes of the optical fiber. For light signals with wavelengths of 1.3 μm to 1.6 μm in single mode fibers, the Brillouin frequency shift is about 9 GHz to 13 GHz. The Brillouin frequency shift increases approximately linearly with increasing tensile strain or temperature when the temperature is not very high (< 400 °C). However, after the optical fiber is exposed to high temperatures, the linear relationships are not satisfied and must be modified [7].

Extrinsic Fabry-Perot Interferometric Sensor

An EFPI sensor typically consists of two parallel reflecting surfaces, which are separated by a cavity, as illustrated in Figure 1. Interference occurs between the multiple reflections of light between the two reflecting surfaces. The reflection spectrum of an EFPI can be described as the wavelength dependent intensity modulation of the input light spectrum [6], which is mainly caused by the optical phase difference between two reflected light beams. Constructive interference occurs if the reflected beams are in phase, and this corresponds to a high-transmission peak. If the reflected beams are out-of-phase, destructive interference

occurs and this corresponds to a reflection minimum. Whether the multiply reflected beams are in phase or not depends on the wavelength (λ) of the incident light (in vacuum), the angle with which the incident light travels through the reflecting surfaces (θ), the physical length of the cavity (L) and the refractive index of the material between the reflecting surfaces (n).

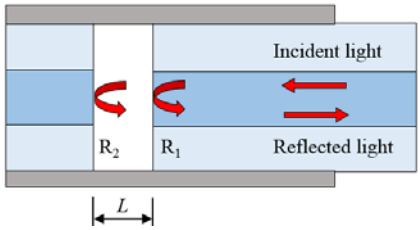

Figure 1. Illustration of a typical EFPI.

The phase difference between each reflected pair of the EFPI is given as:

$$\phi = \frac{2\pi}{\lambda} 2nL\cos(\theta) \tag{1}$$

When perturbation is introduced to the EFPI, the phase difference is influenced with the variation in the optical path length difference of the interferometer. Applying longitudinal strain to the EFPI sensor, for instance, changes the physical length of the cavity, which results in phase variation. By measuring the shift of the wavelength spectrum, the applied strain can be quantified.

EXPERIMENTAL PROGRAM

Test Specimens and Setup

Three S3×5.7 "I-shaped" steel beams were tested with a three-point bending setup in a compartment fire ('flame channel') as shown in Figure 2. Combined temperature and mechanical loading was applied. The three test beams were designated Beam #1, Beam #2, and Beam #3. Each of the beams had a 76 mm depth, 59 mm width, and 1420 mm length. The cross sectional area was 1077 mm^2.

A flame channel, which consisted of a burner rack, an enclosure, and a specimen loading system, was located under a 6 m × 6 m (plan) exhaust hood. The burner rack had four natural gas diffusion burners made of sheet metal, and each of the burners was 300 mm × 300 mm × 140 mm (length × width × height) in dimension. Natural gas entered a burner from the bottom, filled the burner cavity, and then, passed through a ceramic fiber blanket to distribute the gas. The burners were manually regulated by the energy content of the supplied gas, which was measured with an expanded uncertainty of less than 2.4 % [10]. An enclosure constructed of square tube steel, cold-formed steel C-profiles and gypsum board lined with thermal ceramic fiber enclosed the space above the burner rack. The enclosure was open at three faces: the bottom and the two ends in longitudinal direction of the beam, creating the compartment flame dynamics. The heated "compartment" created by the enclosure was approximately 380 mm × 400 mm × 1830 mm (height × width × length) in dimension. Each test beam was simply

supported on two supports constructed of 1-1/2" Schedule 40 pipe, at a 1250 mm clear span. The specimen was loaded by a U-shape 1/2" Schedule 40 pipe (outer diameter: 21 mm) "loading yoke" at the mid-span. The supporting pipes and loading yoke were cooled with the exiting water temperature controlled to less than 50 °C. Load was transferred to the loading yoke with a pulley system.

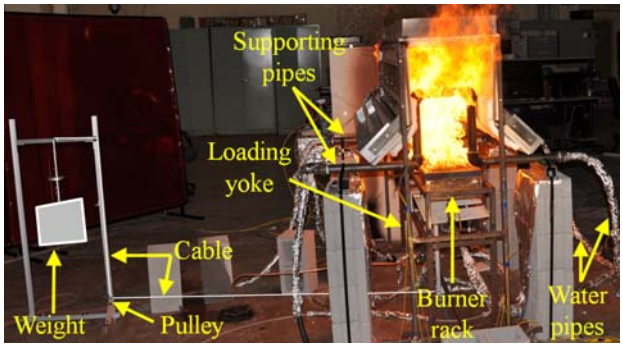

Figure 2. Experimental setup.

Instrumentation of Test Beams

Each beam was instrumented with four glass-sheathed, K-type, bare-bead thermocouples peened into small (diameter < 2 mm) holes, which were drilled into the bottom and top flanges as indicated in Figure 3: TC1 and TC3 at mid-span, and TC2 and TC4 at quarter-span. The thermocouples had a manufacturer-specified temperature standard limit of error of 2.2 °C or 0.75 % (whichever value is greater) over a measurement range of 0 °C to 1250 °C. A calibrated load transducer by Omegadyn was installed on a spanning bar at the bottom of the loading yoke and used to measure the applied load. The linearity and repeatability of the load transducer were ±0.03 % and ±0.01 %, respectively. Each beam was instrumented with one distributed fiber optic sensor (DFO-T) to measure temperature distributions, three distributed fiber optic sensors (DFO-ST1, DFO-ST2, and DFO-ST3) and three EFPI sensors (EFPI1, EFPI2, and EFPI3) to measure strains. The sensors EFPI1, EFPI2, and EFPI3 were closely deployed to DFO-ST1, DFO-ST2, and DFO-ST3, respectively.

Data from the fuel delivery system, thermocouples, displacement sensors and a load transducer were measured continuously using a National Instruments data acquisition system (NI PXIe-1082). Thermocouple data were recorded using 24-bit Thermocouple Input Modules (NI PXIe-4353), and load and displacement data were recorded using a high-speed, 16-bit multifunction module (NI PXIe-6363). Data were sampled at 90 Hz with average values and standard deviations recorded in the output file at a rate of 1 Hz.

A Neubrescope data acquisition system (NBX-7020) for the distributed fiber optic sensors was used to perform PPP-BOTDA measurements with 2 cm spatial resolution and accuracies of 0.75 °C and 15 με for temperature and strain, respectively. In this test, the spatial resolution was 2 cm, meaning that the Brillouin frequency shifts of two points spaced at no less than 2 cm could be distinguished. An optical spectrum analyzer (Yokogawa AQ6370C) was used to acquire data from the extrinsic Fabry-Perot interferometers with a broadband (1470 nm to 1630 nm) light source (Keysight 83437A). The operation wavelength ranged from 1500 nm to 1600 nm. The sampling frequency ranged from 0.2 Hz to 1 Hz.

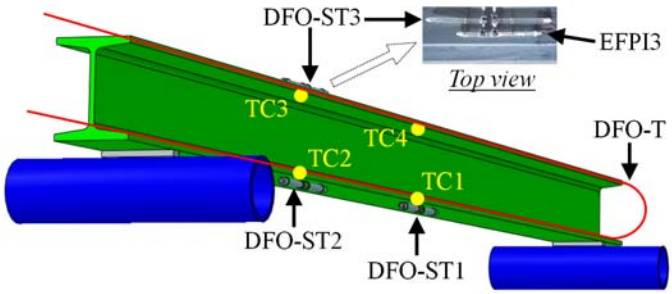

Figure 3. Instrumentation of test beams.

Test Protocol

Each beam was subjected to both fire and mechanical loading. Figure 4 illustrates the fire test protocol.

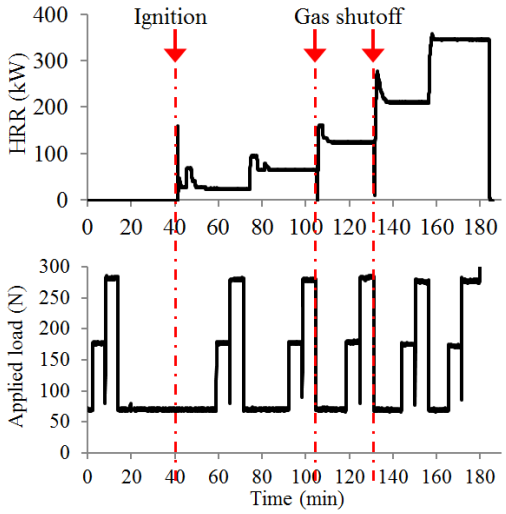

Figure 4. Test protocol.

The heat release rate (HRR) was held approximately constant at five target levels: 25 kW, 65 kW, 120 kW, 195 kW, and 350 kW, which corresponded to beam temperatures at TC1 of approximately 200 °C, 400 °C, 600 °C, 850 °C, and 1050 °C, respectively. During the test of Beam #2, the gas was turned off for about 20 seconds before the HRR was increased to 120 kW and 195 kW, respectively, to allow for visual observation. When the HRR was increased to a higher level, the target value was overshot and then quickly regulated down to the expected value. At each HRR level, in addition to the self-weight, the beam was subjected to three levels of loads at the mid-span. For Beam #1, the three loads were approximately 68 N, 98 N, and 126 N, and sustained for 7 minutes, 4 minutes, and 4 minutes, respectively. For Beams #2 and #3, the three loads were approximately 68 N, 176 N, and 285 N, each sustained for 6 minutes.

EXPERIMENTAL RESULTS AND DISCUSSION

Temperature Measurements

At each sustained HRR level, the beam temperature gradually stabilized to a

temperature with some variation. To quantify the temperature variations, the mean values and standard deviations were calculated over 15 minutes for Beam #1, and 18 minutes for Beams #2 and #3 when the mechanical loads were applied at each temperature level. The coefficient of variation for all the thermocouple readings is less than 4 %. Similarly, to average out the effects of temperature fluctuation, five measurements were made using the DFO-T at each sustained temperature level. Each measurement was an implicit average over a time between 15 seconds and 40 seconds. The DFO-T readings have a maximum coefficient of variation of 4 %, which was similar to that of the thermocouples. The relative difference between the mean temperatures from the DFO-T and the thermocouple ranges from -10 % to 8 %. To understand the statistical significance of the measurement differences, the average of mean temperature differences (four for Beam #1, three for Beam #2, four for Beam #3) was calculated at each HRR level and presented in Figure 5 as an average temperature difference. In addition, the range of mean differences at 95 % confidence level is represented by the error bar.

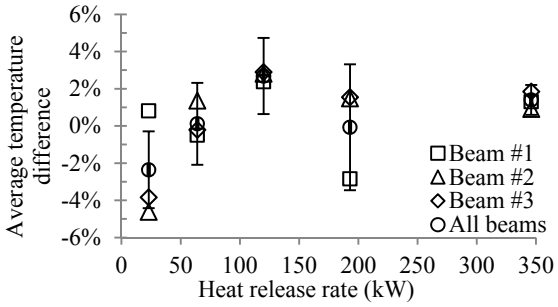

Figure 5. Difference between the fiber optic sensor and thermocouple temperature readings (error bars at 95% confidence).

It can be observed from Figure 5 that the mean difference at 95 % confidence level is less than 5 %, which is acceptable in many engineering applications. The discrepancies may be attributed to several factors. First, the DFO-T sensor was installed in a slightly different location than the thermocouples. Second, the thermocouple beads were located slightly below the surface of the beam and the DFO-T slightly above the surface, and thus, the influence of gas temperature variation on the measurements varied. Additionally, the thermocouples were not corrected for radiation losses.

Strain Measurements

The strain results measured from the EFPI sensors are plotted in Figure 6. As the HRR increases, the strain values approximately linearly increase. When the HRR was no more than 120 kW, the strain results from different sensors attached on different test beams agreed well. At the HRR equal to 120 kW, the strain values were approximately 8000 με to 9000 με. When the HRR became larger than 120 kW, greater variation of the strain results was observed from different sensors deployed at different locations. At the HRR equal to 350 kW, up to 35,300 με (3.53 %) strain was measured by the EFPI sensors.

Similar to the temperature measurements, multiple strain measurements were made from the distributed fiber optic sensors and EFPI sensors at each HRR level. The mean values for the two measurement methods were compared statistically for

the conditions when the HRR was no larger than 120 kW, as shown in Figure 7. The mean strain difference at 95 % confidence level is less than 10 %. There are several reasons for the discrepancy between strain measurements from different sensors. First, the two sensors were deployed at slightly different locations that were subjected to different strains. Second, the data used to calculate the mean values of the two independent sensing systems were not selected at exactly the same moment. Although the two data acquisition systems were synchronized, they had different measurement (reading) durations, and thus, the measurement results were not achieved simultaneously. Third, each instrument has its own accuracy and repeatability at a level, and the measurement results contain error.

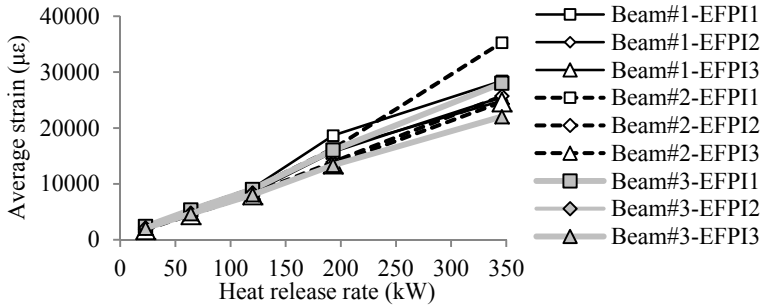

Figure 6. Average strain results measured from EFPI sensors.

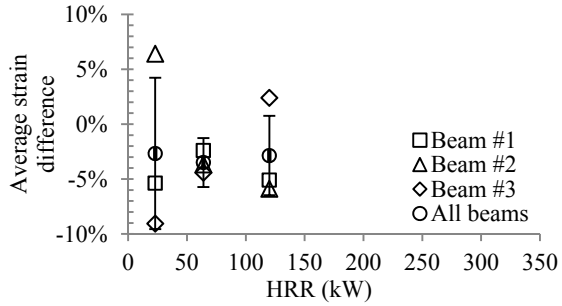

Figure 7. Difference between the distributed fiber optic sensor and EFPI sensor strain readings (error bars at 95% confidence).

CONCLUSIONS

Pulse pre-pump Brillouin Optical Time Domain Analysis distributed fiber optic temperature sensors have been demonstrated at temperatures up to 1050 °C in fire with adequate sensitivity and accuracy for typical structural engineering applications. These measurements add significant value over traditional thermocouples by providing distributed measurements over the length of the optical fiber with a spatial resolution of 2 cm. The measured temperatures were validated by thermocouples resulting in an average relative difference of less than 5 % at 95 % confidence level.

Extrinsic Fabry-Perot interferometric strain sensors have been demonstrated to operate up to 1050 °C in fire and measure at least 35,300 με (3.53 %) strains. The thermal strain predicted from the distributed fiber optic sensor and the extrinsic Farby-Perot interferometric sensor strain results were compared. The mean strain difference at 95 % confidence level was less than 10 %.

These results demonstrate the potential application of fiber optic temperature and strain sensors in structural fire testing. The investigated sensors provide increased temperature resistance, strain capacity, and spatial resolution when compared to traditional methods. Further development of the sensors is required to improve the robustness of the sensors and the speed of installation and measurement.

ACKNOWLEDGEMENT

This work was funded by the National Institute of Standards and Technology (NIST) under Award No. 70NANB13H183. The contents of this paper reflect the views of the authors, and do not necessarily reflect the official views or policies of NIST. Certain commercial equipment, instruments, or materials are identified in this paper to specify the experimental procedure. Such identification is not intended to imply recommendation or endorsement by NIST, nor to imply the materials or equipment are necessarily the best available for the purpose.

REFERENCES

1. Kodur, V., M. Dwaikat, and N. Raut. 2009. “Macroscopic FE model for tracing the fire response of reinforced concrete structures,” Eng. Struct., 31 (10), 2368-2379.
2. Rinaudo, P., B. Torres, I. Paya-Zaforteza, P.A. Calderón, and S. Sales. 2015. “Evaluation of new regenerated fiber Bragg grating high-temperature sensors in an ISO834 fire test,” Fire Safety J., 71, 332-339.
3. Bao, X., and L. Chen. 2011. “Recent progress in Brillouin scattering based fiber sensors.” Sens., 11, 4152-4187.
4. Kishida, K., and C.H. Li. 2006. “Pulse pre-pump-BOTDA technology for new generation of distributed strain measuring system.” Proc. Struct. Health Monit of Intel. Infrastruct., 471-477.
5. Bao, Y., and G. Chen. 2015. “Fully-distributed fiber optic sensor for strain measurement at high temperature.” Proc. 10th Int. Workshop Struct. Health. Monit., Stanford, CA.
6. Rao, Y. J. 2006. “Recent progress in fiber-optic extrinsic Fabry-Perot interferometric sensors,” Opt. Fiber Technol. 12, 227-237.
7. Bao, Y., W. Meng, Y. Chen, G. Chen, K.H. Khayat. 2015. “Measuring mortar shrinkage and cracking by pulse pre-pump Brillouin optical time domain analysis with a single optical fiber,” Mater. Lett. 145, 344-346.
8. Bao Y, G Chen. 2016. “Strain distribution and crack detection in thin unbonded concrete pavement overlays with fully distributed fiber optic sensors.” Opt. Eng. 55(1), 011008.
9. Bao, Y., and G. Chen. 2016. “Temperature-dependent strain and temperature sensitivities of fused silica single mode fiber sensors with pulse pre-pump Brillouin optical time domain analysis,” Mes. Sci. Tech., under review.
10. Bundy, M., A. Hamins, E.L. Johnsson, S.C. Kim, G.H. Ko, and D.B. Lenhert. 2007. “Measurements of heat and combustion products in reduced-scale ventilation-limited compartment fires,” NIST Technical Note 1483.

Author Index

Abbiati, G., 827, 1055
Abboud, N., 604
Abu, A., 700, 933
Achenbach, M., 86, 949
Agarwal, A., 62, 527
Al Hamd, R., 12
Albert, V., 535
Albracht, N., 1124
Alfawakhiri, F., 484
Ali, F., 165
Alos-Moya, J., 743
Anderson, J., 925
Anderson, R., 604
Ando, S., 468
Angelakopoulos, H., 249
Annerel, E., 265
Ashrafi, A., 877
Au, F. T. K., 45
Auguin, G., 675, 1099
Azhari, F., 377
Aziz, E. M., 727

Baba, S., 94
Balasch-Parisi, S., 743
Bamonte, P., 37
Bao, Y., 309, 803
Barnes, A. M., 624
Bartlett, A., 684
Belis, J., 869
Bénichou, N., 3
Berhinig, R. M., 484
Bhatt, P., 153
Bihina, G., 535
Bijlaard, F. S. K., 443
Bilotta, A., 190, 1081
Birely, A. C., 135
Bisby, L., 53, 102, 217, 225, 257, 684
Block, F. M., 901
Boko, I., 1008
Bolina, F. L., 844
Boström, L., 925, 1000, 1016
Brandon, D., 692
Brnic, J., 1008
Buchanan, A., 700
Bundy, M., 803
Burgess, I. W., 1008
Burgess, I., 249, 352, 509
Burnier, O., 885

Cabova, K., 784
Cai, W., 597
Caillet, N., 589
Canadija, M., 1008
Carlton, A., 776
Carter, C. J., 484
Carvel, R., 768
Case, S. W., 811
Case, S., 417
Cashell, K. A., 624
Caspeele, R., 942
Chen, G., 309, 803
Chen, L., 1132
Chen, S. W., 1090
Chen, S., 1047
Chen, X., 1132
Chen, Y., 803
Chen, Z., 1132
Choe, L., 392, 616
Costa, R.-I., 1065
Couto, C., 335, 360
Craveiro, H. D., 408
Cueff, G., 675, 1099

Dai, X., 959
Dao, V. T. N., 257
De Buhan, P., 119
De Silva, D., 1081
De Souza Sollero, M. B., 301
Debuyser, M., 869
Deeny, S., 217
Del Prete, I., 190
Dhakal, R., 933
Di Fiore, D., 190
Divic, V., 1008
Dodangoda, M. T., 1116
Drean, V., 675
Du, Y., 273
Dwiputra, R., 468

El Ghor, A. H., 435
Emberley, R., 643
Engelhardt, M. D., 435, 597
Eslami, M. R., 460
Espinos, A., 535, 552

Felicetti, R., 233, 851
Fernandes, B., 844
Fernando, D., 643
Flint, G., 759
Fontana, M., 241, 293, 819
Frangi, A., 692, 708
Franssen, J.-M., 343, 589, 836, 861
Frost, R. L., 1116
Fu, C., 576

Gales, J., 53
Gambarova, P., 37
Garlock, M. E. M., 727
Garlock, M., 909, 917
Gerlich, H., 700
Gernay, T., 86, 836, 861, 893, 909, 917
Ghisbain, P., 877
Gil, A. M., 844
Gillie, M., 12, 1038
Giuliani, L., 1065
Glassman, J. A., 727
Gonçalves, M., 79
Goremikins, V., 102
Green, M. F., 3
Gross, J., 392, 616

Hadden, R., 684
Hajiloo, H., 3
Han, C., 1132
Han, L.-H., 476
Hantouche, E. G., 435
Hanus, F., 343, 589, 983
Harapin, A., 1008
Häßler, D., 1099
He, S., 425
Heck, J.-V., 119
Heidarpour, A., 324, 377
Hervey, F. E., 484
Hirashima, T., 316, 468, 667
Hiriyur, B., 604
Ho, S. H. D., 249
Hodges, J. L., 811
Hoehler, M. S., 803
Honfi, D., 869
Hospitaler, A., 535
Hothan, S., 1099
Hou, X., 1024
Hozjan, T., 1073
Hrasky, O., 784
Hu, J., 768
Huang, S.-S., 249, 352, 509
Huang, Z., 71
Huczek, J., 1124
Hutchinson, C. R., 377

Igarashi, S., 635
Imai, K., 94
Imani, R., 877

Janssens, M., 1124
Jeffers, A. E., 967
Jeffers, A., 975
Jessop, D., 700
Jiang, J., 368, 492
Jiang, L. M., 1090
Jiang, L., 959, 1047
Jiang, X., 443
Jomaas, G., 1065
Jostrom, J., 869
Just, A., 650

Kahanji, C., 165
Kalaba, N., 37
Katakura, Y., 667
Kato, M., 94
Kawohl, A. K., 452
Khalaf, J., 71
Kho, T.-S., 901
Khorasani, N. E., 909, 917
Kinjo, H., 667

Kleiboemer, I., 544
Knobloch, M., 293, 819
Kodur, V. K. R., 28, 62, 153, 174, 460, 719, 727
Kolpasky, L., 784
Kolstein, H., 443
Korzen, M., 608
Kotsovinos, P., 759, 975

Laim, L., 560
Laim, L. M., 408
Lam, D., 552
Lane, B., 684, 759
Lange, D., 110, 869, 925, 1000, 1016
Lange, J., 452
Lattimer, B. Y., 811
Lattimer, B., 417
Law, A., 209
Le, Q. X., 257
Lelli , L., 517
Li, C., 425
Li, G.-Q., 368
Li, J., 45
Li, X., 309, 1132
Li, Y., 145
Li, Y.-Q., 385
Liew, J. Y. R., 273
Liu, C., 576
Liu, F., 568
Liu, J. X., 1032
Liu, J.-C., 282
Lo Monte, F., 233, 851
Lopes, G. C., 360
Lopes, N., 335, 360
Loutan, J., 517
Lu, F., 241
Lucherini, A., 1065
Lv, H. R., 174

Mackie, K. R., 1055
Maclean, J., 102, 110, 959
Mahendran, M., 1116
Main, J. A., 492
Maluk, C., 209, 217, 225, 257
Mandal, P., 1038
Marjanishvili, S., 751, 776
Martinez, J., 967
Matsagar, V., 153
Matthys, S., 199
Mehal, S., 119
Miah, M. J., 127, 233
Michikoshi, S., 94
Mindeguia, J.-C., 675
Mirmomeni, M., 324
Molkens, T., 893
Moreno, Jr., A. L., 301
Morgenthal, G., 86, 949
Morovat, M. A., 435
Moss, P., 933
Mueller, K., 751, 776

Nadjai, A., 165, 343
Nagaoka, T., 635
Naser, M. Z., 719
Neuenschwander, M., 293, 819
Ni, S., 135
Nicolaidis, A., 643
Nigro, E., 190, 1081

Ohashi, H., 635
Olsson, K., 1016
Ožbolt, J., 20

Packer, J. A., 324
Palma, P., 708
Palmieri, A., 199
Pargeter, R. J., 624
Paya-Zaforteza, I., 743
Periškiæ, G., 20
Peris-Sayol, G., 743
Pham, D. T., 119
Pilakoutas, K., 249
Pimienta, P., 127, 233
Pinoteau, N., 127
Poologanathan, K., 1116
Poormohamadi, A., 460
Possidente, L., 827
Proia, A., 199

Qi, S. L., 174
Qiang, X., 443
Quan, G., 352
Quichaud, F., 509
Quiel, S., 751, 776

Rackauskaite, E., 110, 975
Ramalho, M. A., 79
Ramesh, S., 392
Razzazzadeh, A., 476
Real, P. V., 335, 360
Rein, G., 975
Ren, C., 425
Ren, P., 1024

Renaud, C., 535
Rezaeian, A., 460
Rickard, I., 217
Rippe, C., 417, 811
Robert, F., 836
Rodrigues, E. E. C, 844
Rodrigues, J. P. C., 408, 560
Romero, M. L., 535, 552
Rong, Q., 1024
Rush, D., 110
Ryjacek, P., 784

Sadek, F., 492
Saito, K., 667
Saje, M., 1073
Sanad, A., 768
Santomaso, A., 692
Sanzel, A., 335
Sauca, A., 836
Scandella, C., 293
Schaumann, P., 544
Schmid, J., 692
Schulthess, P., 819
Shakya, A. M., 28
Shen, Z.-Y., 385
Siemon, M., 791
Smith, C. M., 803
Smith, H., 12
Sonck, D., 869
Song, T.-Y., 476
Spearpoint, M., 700
Stojadinovic, B., 827, 1055
Stratford, T., 12, 102
Sultan, M., 3
Sun, R. R., 501

Taddhanpally, S., 527
Taerwe, L., 199, 265, 942
Tan, K. H., 145, 282, 1032
Tao, Z., 476
Tattoni, S., 37
Terrasi, G. P., 225
Thauvoe, C., 983
Tian, K., 20
Tiso, M., 650
Tondini, N., 343, 827, 836, 983
Torelli, G., 12, 1038
Torero, J. L., 209, 257, 643
Toric, N., 1008
Tran, V.-X., 1038
Treven, A., 1073
Turkalj, G., 1008
Tutikian, B. F., 844

Usmani, A. S., 1090
Usmani, A., 768, 959, 1047
Uzelac, I., 1008

Van Coile, R., 893, 942
Van Den Steen, T., 265
Vassart, O., 343, 589
Vujtech, J., 784

Wade, C., 700
Wald, F., 784
Walker, G., 759
Wang, L., 942
Wang, Y. J., 1090
Wang, Y., 12, 576
Wang, Y.-H., 385
Wei, Y., 45
Weigand, J. M., 492
Welch, S., 959
Werther, N., 650
Whyte, C. A., 1055
Wickstrom, U., 692
Winful, D. A., 624
Woelke, P., 604
Wong, B. V. Y., 501
Woods, L. C., 484

Xiong, M., 273
Xu, D., 576
Xu, L., 400
Xu, Q., 1132

Yahyai, M., 460
Yamashita, H., 316
Yang, H., 568
Yang, M., 119
Yang, S., 400
Yoshida, T., 316
Yusa, S., 667

Zeeveld, P., 484
Zehfuß, J., 791
Zhan, Y., 1024
Zhang, C., 392, 616, 992
Zhang, H. Y., 174
Zhang, H., 309
Zhang, L., 45
Zhang, S., 568

Zhao, B., 335, 983
Zhao, X., 425
Zhao, X.-L., 324, 377
Zheng, W., 1024
Zhu, Z., 776